International Journal of
Advanced Structural Engineering
a SpringerOpen Journal

CONTRIBUTED RESEARCH   **Open Access**

Geometrical metallic shell behavior study under compression

Ram Ranjan Sahu[1,3*] and Pramod Kumar Gupta[2]

Abstract

The loading response of shell structures depends on their shapes. The individual shape behaves uniquely to the loading, and different shapes give different load displacement graphs. If these geometries are combined, then their load displacement graphs can be different. It may happen that their combined behavior can be harnessed to be used as better energy absorber in a controlled manner, which they cannot if they are used individually. Experiments were conducted on two separate geometries as well by joining them with weld. The first geometry was the top cylindrical and frusta bottom. The second geometry was the shape of inverted bell crater and half-spherical shells. Combining these two shapes produced the third geometrical shape. The large deformation was obtained by crushing these geometrical shells between two flat plates. The finite element analysis was used to simulate the crush phenomenon. The behavior of the geometrical shell to large deformation was understood with load displacement graph for different samples. The energy absorbed by the different samples was calculated and compared. The parameters, like material and thickness, were varied for the samples to see their effect on the large deformation behavior. Moreover, friction role is discussed on the crush phenomenon. This paper also gives an idea on the different parameters which can affect the energy-absorbing capacity of the combined geometrical shells.

Keywords: Geometrical shell, Crushing, Large deformations, Energy absorption, Load-deflection, Finite element analysis

Introduction

Shell structures are good energy absorbers and have been attracting researchers to study their response for large deformation. In day-to-day life, many types of shell structures are being used in construction. These shell structures could be a combination of many shell geometries. It can be a combination of cylinder, frusta, spherical shells, etc. Many researchers tried to understand these shells under different loading conditions. The collapse behavior of thin spherical shells under quasi-static loading was studied by Gupta et al. (2008). Three-dimensional numerical simulations were carried out for all the specimens tested under quasi-static loading using ANSYS (ANSYS, Inc., Canonsburg, PA, USA). All the stages of collapse of the shell including nonsymmetrical lobe formation were simulated. Material, geometric, and

contact nonlinearities were incorporated in the analysis. The obtained results were compared with the experiments. They investigated that the relatively thick shells deform axi symmetrically and the major load is absorbed by the rolling plastic hinges. When the thickness is reduced considerably, the inward dimpling is followed by multiple numbers of nonsymmetrical lobes which are caused by the formation of stationary hinges. Deformations and energy absorption capacity of thin-walled tubes with various section shapes (circular, square, rectangular, hexagonal, triangular, pyramidal, and conical) were investigated both experimentally and numerically by Nia and Hamedani (2010). The tubes with same volume, height, average section area, thickness, and material were subjected under axial quasi-static loading. They found that the section geometry has considerable effect on the energy absorption. The larger the number of section edges, the greater is the energy absorption capacity. This is due to an increase of the number of folds and plastic hinges in sections with larger number of edges. For their test, the absorbed energy per

* Correspondence: RamRanjan.Sahu@tatatechnologies.com
[1]Civil Engineering Department, Indian Institute of Technology Roorkee, Uttarakhand Pin 247667, India
[3]Engineering Research Centre, Tata Motors-Pune, India
Full list of author information is available at the end of the article

unit mass was maximal for cylindrical tubes. Postlethwaite and Mills (1970) studied the frustum and proposed the mean crushing force calculation for external collapse. The failure modes of frusta with experiments were studied by Mamalis and Johnson (1983). They found that the load-deflection curves of the frusta were more regular than those of the cylinders. It was also observed that with the increase in wall thickness, the post-buckling load increased in a parabolic manner. They also observed that the post-buckling load decreased with an increase in semi-apical angle. It was also observed that the thin frusta deformed in diamond shape while the thick ones deformed into axisymmetric rings. Alghamdi (1991) worked on direct inversion and outward flattening for frusta. Abaqus finite element program (Dassault Sytemes, Veilizy-Villacoublay, France) was used by Aljawi and Alghamdi (1999) to simulate the frusta inversion process. They found a good agreement between the finite element (FE) and experimental results. The collapse studies on varying wall thicknesses of the metallic frusta subjected to axial compression were done by Gupta (2008). The mode of collapse forms by the development of one concertina fold followed by the plastic zone. During the development of mode of collapse, some portions of the frusta move radially inward and some radially outward. Experimental investigation for axial compression of thin-walled circular tubes was done by Guillow et al. (2001). Alghamadi (2001) paper reviews the common shapes of collapsible energy absorbers and their
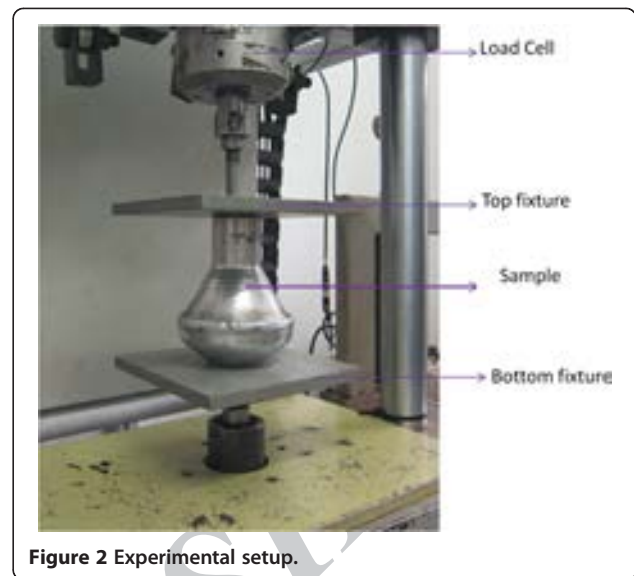

Figure 2 Experimental setup.

different modes of deformations. The typical geometrical shell studied for large deformation behavior is shown in Figure 1.

Experiments

Experimental setup

The experimental setup consists of rigid top and bottom fixtures and aluminum samples as shown in Figure 2. Aluminum samples are compressed between these two rigid fixtures through Instron Universal Machine (Instron, Norwood, MA, USA).
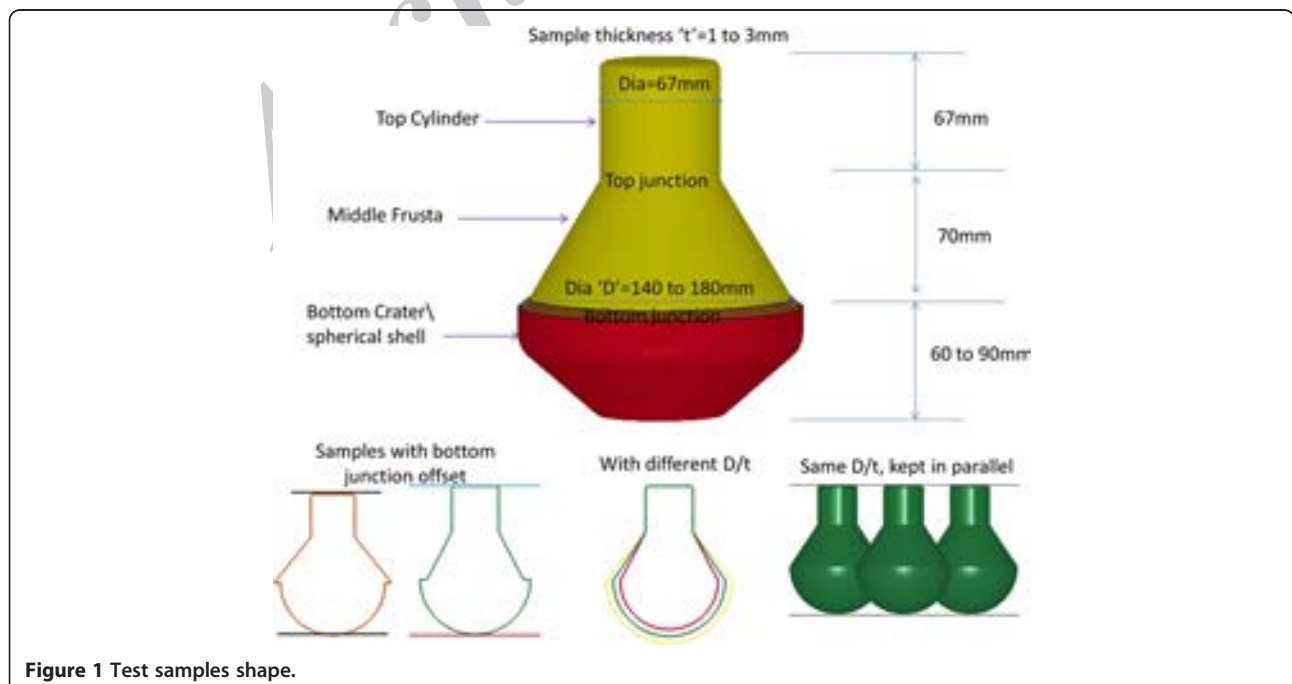

Figure 1 Test samples shape.

Figure 3 Experimental samples.

The aluminum samples were made by spinning process. The top half and bottom half were made separately. The both the halves were joined by aluminum weld. Top and bottom samples are shown in Figure 3 before and after joining.

The typical shape of the top half is a combination of cylinder and frusta. The bottom half is of inverted bell crater shape, and few samples were with spherical shapes. After joining the two halves, junctions are formed, namely, top and bottom junction. The typical dimensions and parametric models are shown in Figure 1.

The top fixture is fixed to load cell of the Instron machine and is stationary. The bottom fixture is attached to moving ram of the machine. The sample is held between these two fixtures. The Instron machine has a maximum capacity up to 4 ton. The load cell is kept below the top stud. The bottom ram moves up and down with the maximum ram stroke up to ± 125 mm. The system is hydraulically operated and can operate at quasi-static and transient load conditions. The ram on which tube is kept was moved up with speed of 5 mm/min to ensure the quasi-static condition. The alignment of the sample and its fixture is assured with the machine axis. The testing was done to the maximum displacement up to 150 mm.

Material properties

The tensile testing of the material was done by preparing test specimens as per ASTM E8 (American Society for Testing and Materials, West Conshohocken, PA, USA) specifications, as shown in Figure 4a. These test specimens were cut from the samples. These test pieces were tested with standard tensile testing machine at room temperature. A specimen after test is shown in Figure 4b. With repeated test, the average value of stress strain is shown in Figure 4c. From the graph,
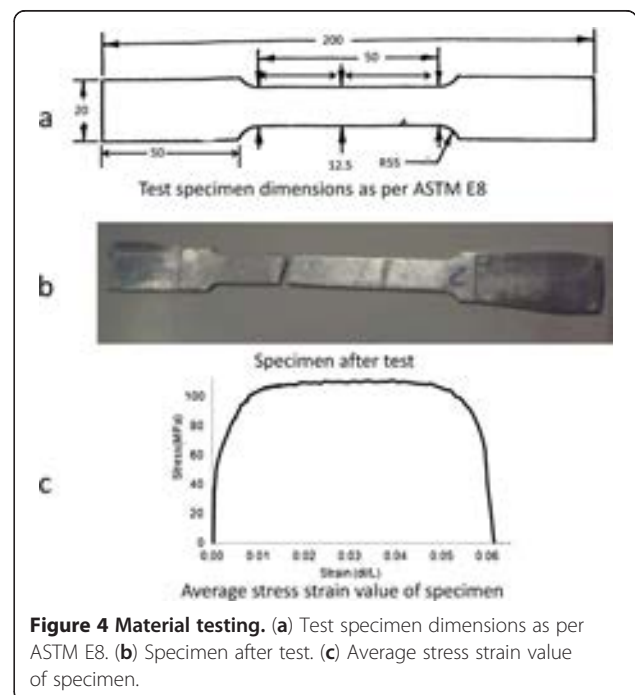

Figure 4 Material testing. (**a**) Test specimen dimensions as per ASTM E8. (**b**) Specimen after test. (**c**) Average stress strain value of specimen.
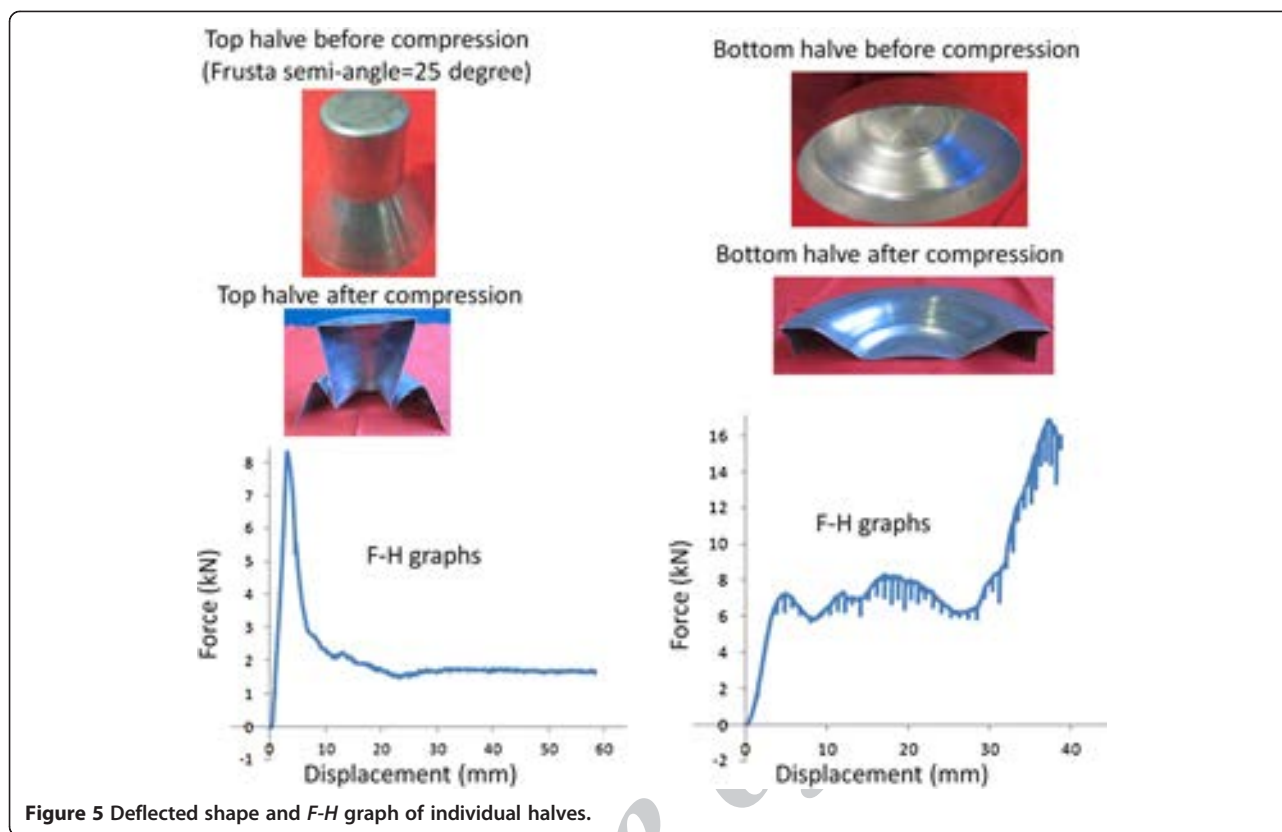
Figure 5 Deflected shape and *F-H* graph of individual halves.

material properties (tensile strength = 108 MPa at 4.6% strain and yield strength = 65 MPa) were extracted as per ASTM E8 standards.

The fixtures were made of steel having 0.2% proof stress of 800 MPa and an elastic modulus of 210 GPa. Since proof stress of fixture is much greater than that of the samples, it can be regarded as rigid.

Experimental results

The experiments were conducted on individual halves as well on combined geometry samples. Figure 5 shows the shape before and after compression and their respective force-displacement (*F-H*) graph. The unit followed for force was in kilonewton (1,000 N) in *y*-axis and displacement in millimeters at *x*-axis. The top half of the sample mainly shows the inward inversion of frusta portion, while inward dimpling is shown for bottom half of the crater. For the energy calculation for the bottom half, the portion with sudden rise in the *F-H* graph is not taken.

The typical behavior of the combined geometrical shell can be explained by Figure 6, where deflected shapes are also shown in different stages of the graph. The *F-H* graph starts from point 1 till it achieves the maximum force to point 2. This is the force requirement for the geometry to start the process of plasticity. This force starts the inward inversion of frusta

portion of top half and inward dimpling of bottom half. Once this process starts, the graph drops down and stabilizes and goes up to point 3. After this point, the inverted frusta and bottom dimpled halves contact each other, which resulted into increases in force which is denoted by point 4.
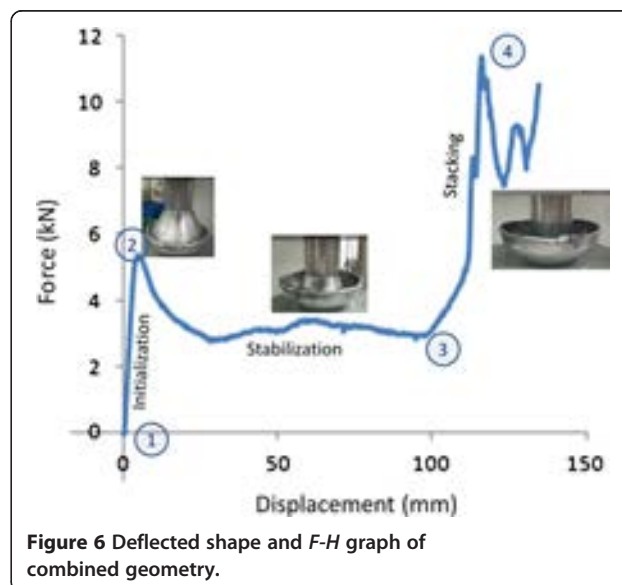

Figure 6 Deflected shape and *F-H* graph of combined geometry.

Table 1 Sample categories and their results

Category	Sample geometry	Sample description	Sample number	Parameter	Stroke (*H*) (mm)	Energy (kJ)	Weight of the sample (kg)	ω = (kJ/kg)	Average *F* (kN)
Experimental	Separate geometry	Bottom half only	S1	Shape, bell crater	38.78	0.196	0.092	2.13	5.05
		Top half only	S2	Frusta semi-angle = 25°	58.28	0.123	0.0825	1.49	2.11
	Combined geometry	Frusta semi-angle = 30° (sample 30_1)	S3	Crater bottom half, bottom junction mean diameter = 154 mm	144.59	0.543	0.198	2.74	3.76
		Frusta semi-angle = 30° (sample 30_2)	S4	Crater bottom half, bottom junction mean diameter = 156 mm	140.68	0.699	0.198	3.53	4.97
		Frusta semi-angle = 30° (sample 30_3)	S5	Crater bottom half, bottom junction mean diameter = 155 mm	148.50	0.71	0.198	3.59	4.78
		Frusta semi-angle = 25° (sample 25_1)	S6	Crater bottom half, bottom junction mean diameter = 147 mm	114.50	0.2088	0.191	1.09	1.82
		Frusta semi-angle = 25° (sample 25_2)	S7	Spherical bottom half, bottom junction mean diameter = 140 mm	157.00	0.641	0.202	3.17	4.08
Theoretical (base sample with bottom junction diameter = 160° and *t* = 1 mm)	Combined geometry	Different offset	S8	Offset_out10	150.00	0.61	0.263	2.32	4.07
			S9	Offset_in10	150.00	0.57	0.236	2.42	3.80
		Different '*D* / *t*'	S10	*D* / *t* = 140	150.00	0.879	0.198	4.44	5.86
			S11	*D* / *t* = 160	150.00	0.742	0.235	3.16	4.95
			S12	*D* / *t* = 180	150.00	0.626	0.277	2.26	4.17
		Different '*μ*'	S13	*μ* = 0.1	150.00	0.742	0.235	3.16	4.95
			S14	*μ* = 0.2	150.00	0.638	0.235	2.71	4.25
			S15	*μ* = 0.3	150.00	0.583	0.235	2.48	3.89
		Different '*t*'	S16	*T* = 1 mm	150.00	0.742	0.235	3.16	4.95
			S17	*T* = 2 mm	150.00	2.18	0.47	4.64	14.53
			S18	*T* = 3 mm	150.00	3.22	0.706	4.56	21.47
		Different 'material'	S19	Tested	150.00	0.742	0.235	3.16	4.95
			S20	Mat 1050 (m1)	150.00	0.483	0.235	2.06	3.22
			S21	Mat 6082 (m2)	150.00	2.11	0.235	8.98	14.07
			S22	Mat 7020 (m3)	150.00	3.01	0.235	12.8	20.07
		Different lattice	S23	Single sample	150.00	0.596	0.194	3.07	3.97
			S24	Three samples in parallel	150.00	1.78	0.584	3.05	11.87

Figure 7 Step for analytical analysis.
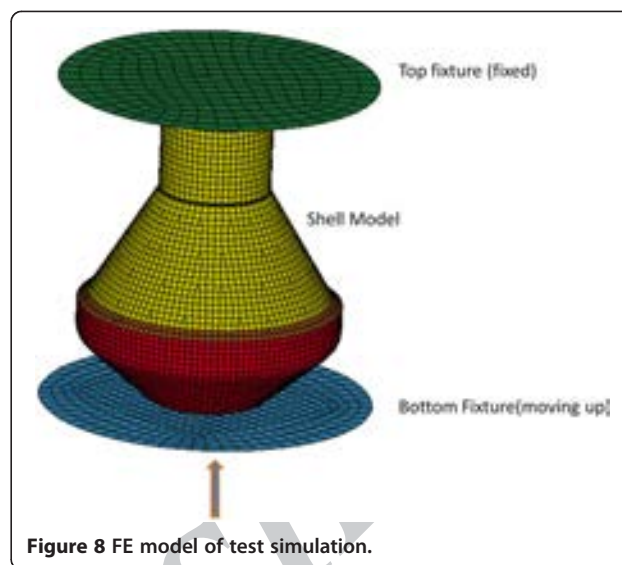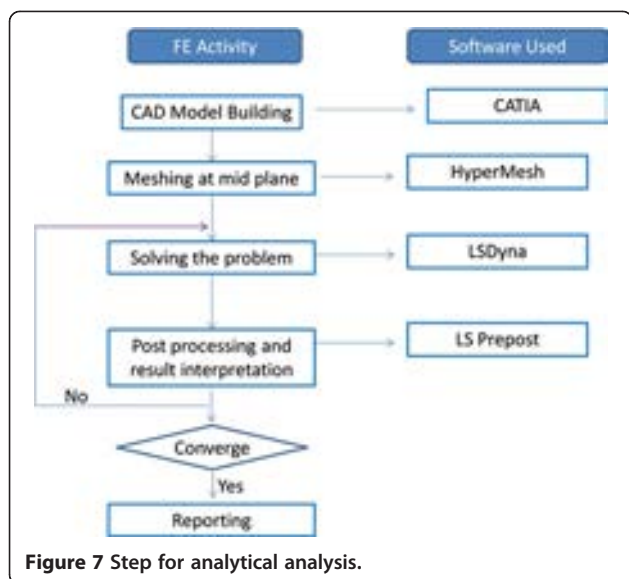

Figure 8 FE model of test simulation.

Table 1 contains the geometrical parameter details, energy contents, specific energy, average force for the sample tested along with the analytical sample results. From the table, it is evident that the specific energy (ω) reduces with the offset and higher D / t ratio at bottom junction. It also reduces with higher coefficient of friction while increases in higher strength material. The average force is observed to be maximal for higher-thickness and higher-strength materials.

Finite element simulation
The analytical approach for test simulation is discussed below. The step followed for analytical analysis is shown in Figure 7.

The sample computer-aided design (CAD) models were made in CATIA software (Dassault Sytemes, Veilizy-Villacoublay, France). Once the CAD models are ready, their middle surface can be extracted for FE model building. HyperMesh (2011) was used for FE model building. Aluminum samples were represented with shell elements at their middle surface. Triad and quad shell elements were used for FE model building. The element sizes chosen were fine enough to fully represent the details of geometry, like small curved fillets. The top and bottom fixtures were represented with rigid elements. The LsDyna (Livermore Software Technology Corporation 2003) explicit solver was used to solve the problem. The material models *MAT_RIGID and *MAT_PIECEWISE_LINEAR_PLASTICITY were used for fixtures and samples, respectively. The contact type *CONTACT_AUTOMATIC_SURFACE_TO_SURFACE was used to define contacts between disjoint parts. Also, for self-contact, *CONTACT_AUTOMATIC_SINGLE_

SURFACE was used. Coulomb friction type was used to define the coefficient of friction between samples and fixtures. Shell element formulation chosen was Belytschko-Tsay because of its less computation cost with good accuracy. FE model fully represents the sample and simulates the compression process. Result interpretation was done through LS-PREPOST (Livermore Software Technology Corporation 2007). Figure 8 shows the FE shell model of test simulation.

Theoretical analysis confidence on correct simulation to test was established and with this confidence, the various parametric theoretical samples were prepared. The base sample diameter at bottom junction for theoretical models is kept at 160 mm for all types of parametric models except for samples in which the D / t values are 140 and 160. The parameters could be offset at the bottom junction, different D / t, different coefficients of friction, different thicknesses, different materials, samples lattice, etc. These theoretical samples are enlisted in Table 1 and their results are discussed.

The tested sample S3 was simulated with FE as shown in Figure 9. The deflected shape and their *F-H* graph compared well. This shows the FE assumptions and material test data taken in analysis are correct.

The energy balance graph of FE simulation for sample S3 is shown in Figure 10. The undesired energies like kinetic energy, hourglass energy, and sliding energy are minimal (less than 10% of the total energy) and hence, the total energy is contributed only through sample internal energy which is caused by the deformation. The graph represents a perfect energy balance of simulation and hence ensures the correctness of simulation and convergence. Also, this
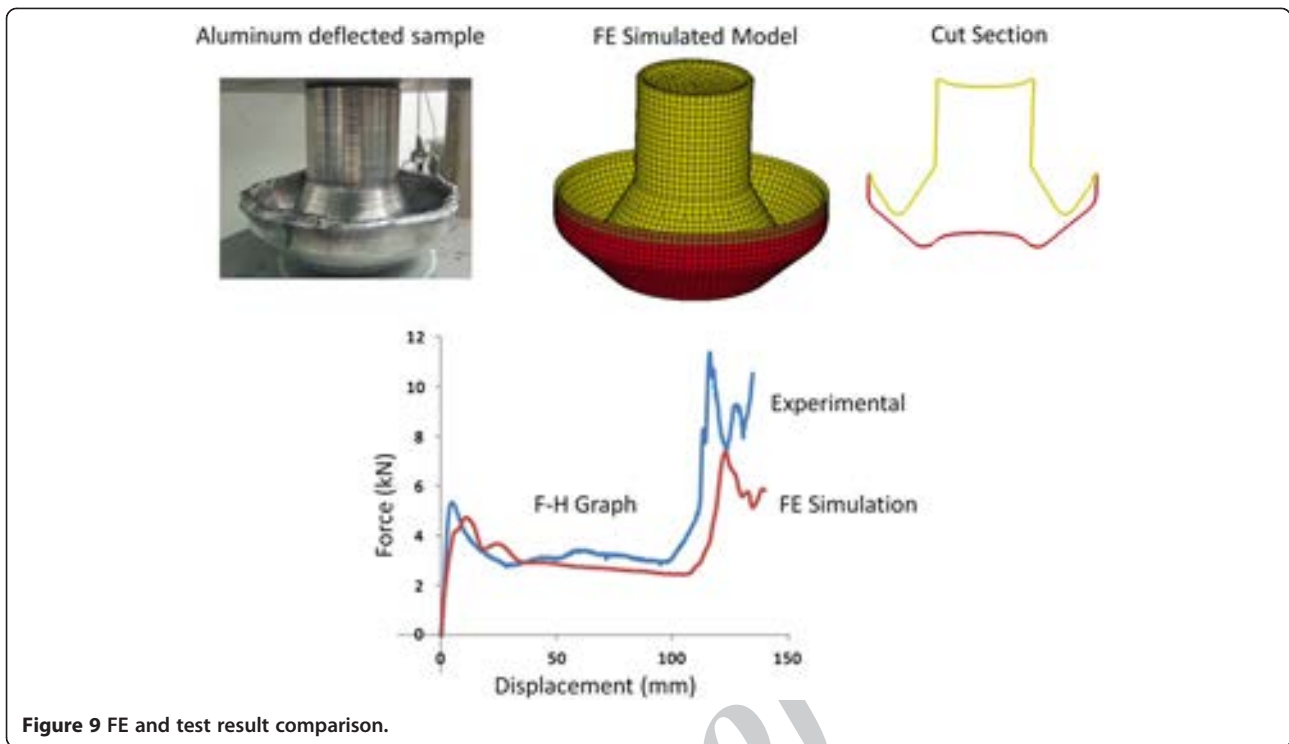
Figure 9 FE and test result comparison.

energy balance graph gives confidence on the element type chosen and on its formulation.

Results and discussion

The FE-simulated *F-H* graph and von Mises stress contour for sample S3 at different deformation stages are shown in Figure 11. The stress contour in red colored which indicates the plasticity of metal, is depicted for rolling hinges formed due to inward inversion of frusta portion at *H* = 70 mm. Contours at the last stage of deformation is also shown where the top cylindrical portion has undergone plasticity. Hence, by plotting stress contour at different deformation stages, the relative plasticity of the different portions of the sample can be assessed.

The *F-H* graph and cut section of sample S8 (outward 10 mm offset) is shown in Figure 12. The initial rising portion of the graph is due to the inward dimpling of bottom spherical shell which continues up to *H* = 45 mm. Further enforced displacement starts necking, and sudden drop in *F-H* graph is noticed. This necking initiates the inward inversion of conical portion until it reaches *H* = 125 mm. Afterwards, the bottom spherical and inward inverted portions touch each other, leading to a sudden jump in effort. This shows that the outward offset at bottom junction
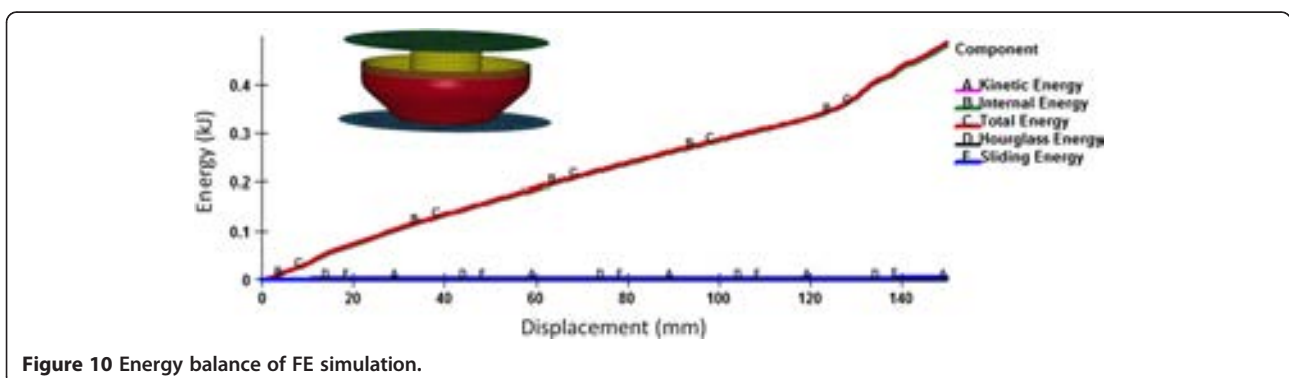
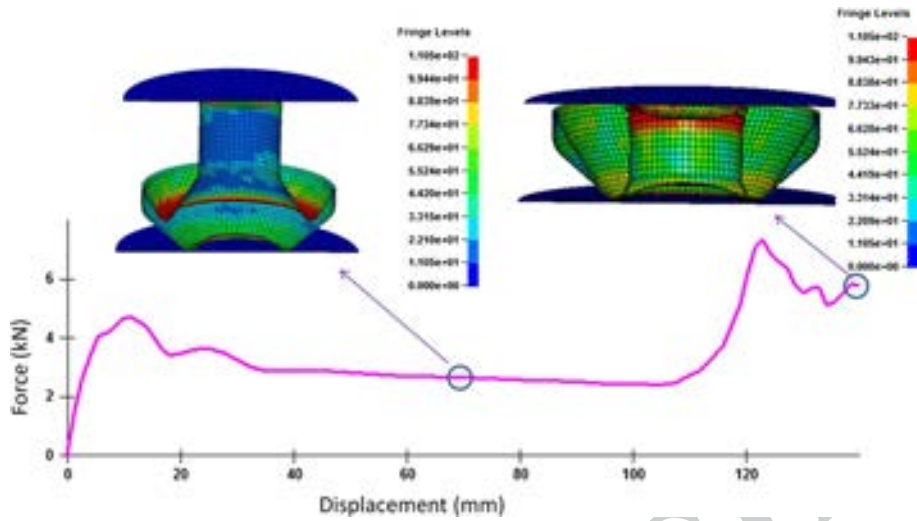**Figure 10** Energy balance of FE simulation.

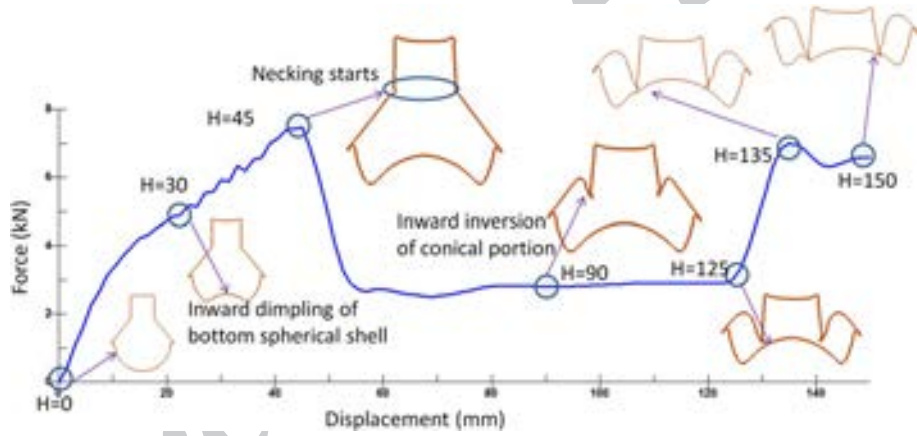**Figure 11** FE-simulated *F-H* graph and stress contour.

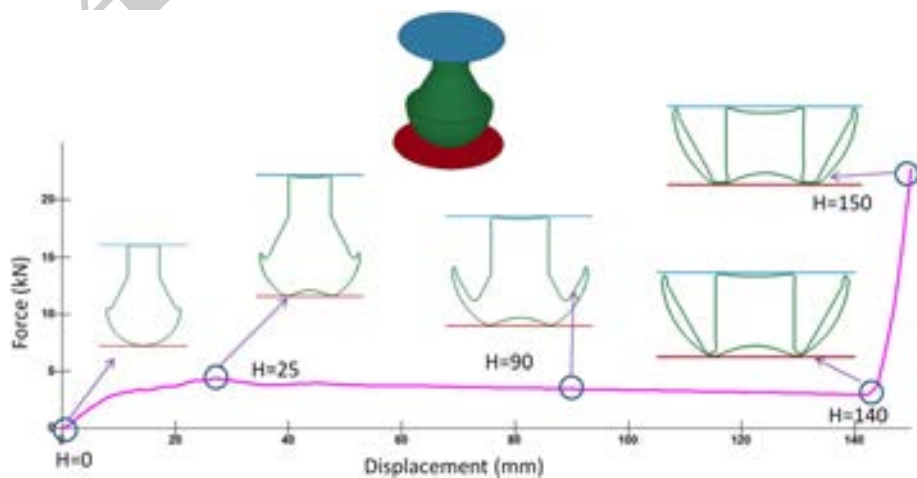**Figure 12** *F-H* graph and deflected cut section for sample S8.

Figure 13 *F-H* graph and deflected cut section for sample S9.
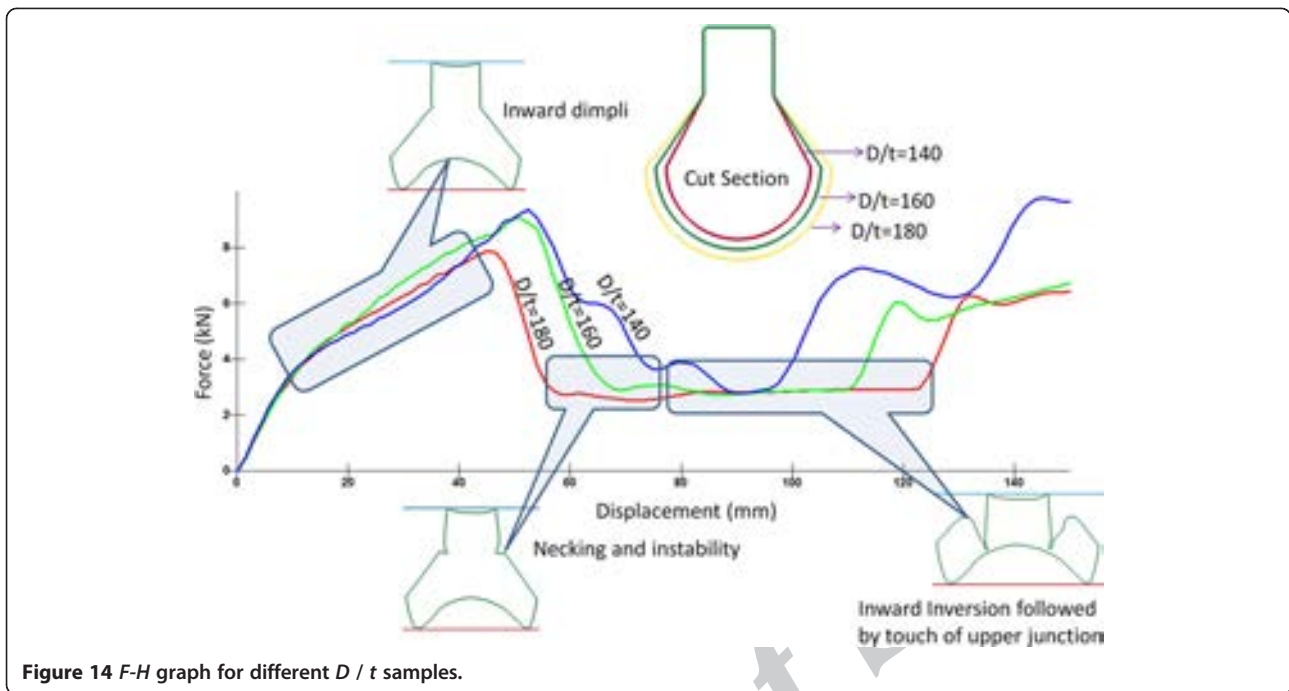
Figure 14 *F-H* graph for different *D* / *t* samples.

leads to inward dimpling first, followed by necking and inward inversion of conical portion.

The *F-H* graph and deflected cut section at different stages of deflection for sample S9 (inward 10 mm offset) are shown in Figure 13. The initial rising portion of the graph is due to the inward dimpling of bottom spherical shell and setting plasticity at the offset which happens at *H* = 25 mm. Afterwards, the conical portion is inverted from its bottom to the upper portion. In this process the rolling hinges volume

decreases and hence the *F-H* graph trend declined. This inversion continues until point reaches *H* = 140 mm. Afterwards, the bottom of the top cylindrical portion touches to dimpled spherical portion, causing rise in the effort. In this whole process, the bottom spherical and top cylindrical portions are not utilized effectively. The inward dimpling at the bottom junction provokes the inversion, and this featured phenomenon could be used in large deformation applications.
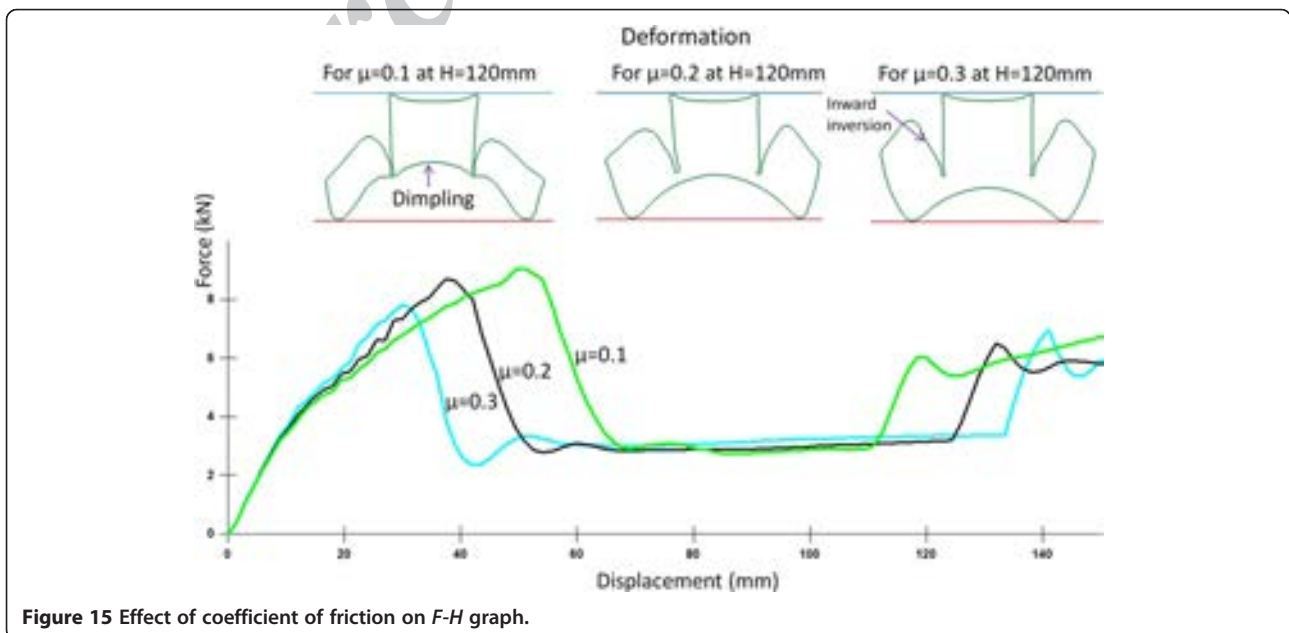

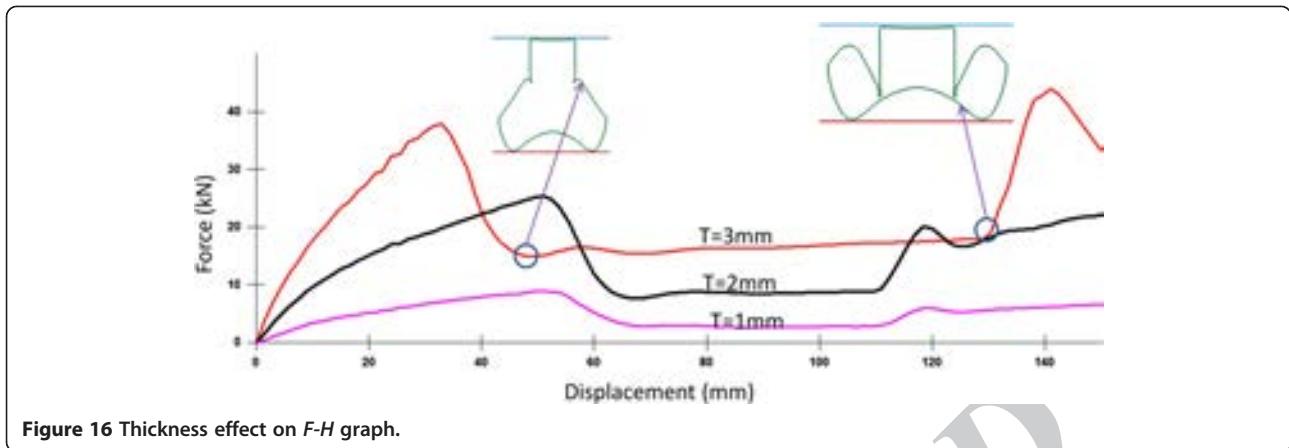**Figure 15** Effect of coefficient of friction on *F-H* graph.

Figure 16 Thickness effect on *F-H* graph.

Three samples (S10, S11, and S12) were made with *D* / *t* ratios at bottom junction as 140, 160, and 180. The superimposed graphs of these three samples are shown in Figure 14. The graph for all three samples rises to approximately 50 mm of stroke, which is mainly due to inward dimpling of bottom spherical shell. After further application of the enforced bottom plate motion, the necking starts at the top junction (also some instability occurs at the bottom junction for *D* / *t* = 140) which leads to a sudden drop in *F-H* graph. Afterwards, the inward inversion of the middle frusta starts. On further displacement of the bottom plate, the top junction touches to the dimpled bottom spherical shell and, hence, the force suddenly increases. The bottom junction continues to press the bottom spherical shell until it reaches *H* = 150 mm. The wide stretch in the graph is noticed for inward inversion of middle frusta for *D* / *t* = 180 while it is less for *D* / *t* = 140. The higher *D* / *t* ratio renders more inward inversion of the middle frusta while the lesser *D* / *t* ratio in the sample does not; however, instability is noticed in the frusta portion.

The effect of coefficient of friction *μ* between contacts was studied on the samples S13, S14, and S15 who have the same shape with *D* / *t* = 160 at the

bottom junction. Figure 15 shows superimposed *F-H* graph for samples of *μ* = 0.1, 0.2, and 0.3. It is clear from the figure that at higher coefficient of friction, the inward dimpling is reduced due to the higher friction at the bottom, which invokes the early start of inward inversion of the middle frusta. With lesser value of coefficient of friction, it is reversed where inward dimpling is allowed more than the frusta inward inversion.

The effect of thickness was studied on samples S16, S17, and S18, and the *F-H* graph of these samples is shown in Figure 16. The samples were with mean diameter of 160° at the bottom junction and their thicknesses were varied from 1 to 3 mm. The larger thickness has difficulty in inward dimpling, and hence early necking followed by inversion starts. Therefore, the higher thickness sample shows large stretch for inward inversion of the frusta portion. Also, higher thickness yields more energy (see Table 1).

Three types of aluminum alloy along with tested materials have been used, i.e., high, medium, and low strengths to see the material effect on the deformation pattern. The properties are enlisted in Table 2.

The examples of high strength alloy are 7xxx, e.g., 7020 and 7075, and they are comparable to high-strength steel. The medium strength alloy is 6xxx series; for example, 6082. Their strength is comparable to mild steel. The low-strength aluminum alloy could be in the pure form of aluminum, for example, 1050A and 1050-O. The geometrical sample for this study was taken as *D* / *t* = 160 at bottom junction and these were assigned with four types of material properties. The samples are S19, S20, S21, and S22 as shown in Table 1. The shape of *F-H* graph along with the deformation pattern at 50% and 100% of compression is shown in Figure 17. The material having lower strength facilitates the inward inversion of frusta portion, while it shows instability for

Table 2 Material properties

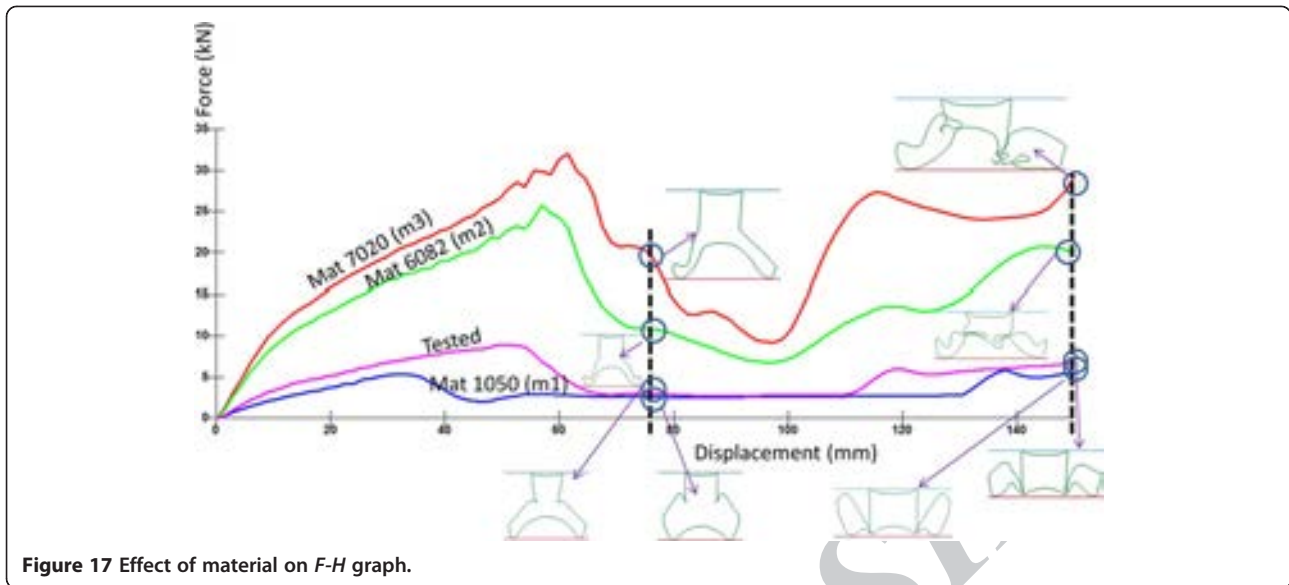| Material name	Properties		
	Tensile strength (MPa)	Yield strength (MPa)	Elongation (%)
Tested	108	65	4.6
m1 (1050)	130	60	20
m2 (6082)	340	310	11
m3 (7020)	430	420	11

Figure 17 Effect of material on *F-H* graph.

samples with higher strength materials. Also looking at the last stage deformations, the pattern is regular for samples of lower strength materials, while it is of irregular pattern for samples with strength materials.

The energy (kJ) bar chart for samples of different materials are plotted in Figure 18, for 7020, 6082, tested, and 1050 materials whose yield values are highest to lowest, respectively. The 7020 alloy has the maximum yield value as compared to all and which gives the highest value of energy in its sample, while 1050 gives the least. Hence, it can be said that the material having higher yield value will have more deformation energy keeping other the same condition.

The samples S23 and S24 were prepared to study the effect of samples lattice on load displacement pattern. The sample S23 was a single sample (D / t = 160), while S24 has three numbers of S23 kept in parallel.
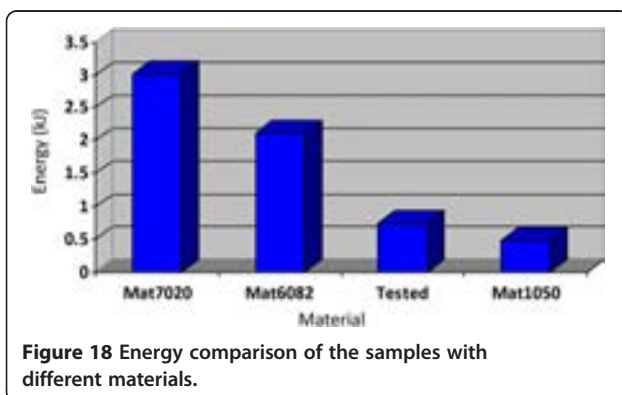
The effect could be clearly seen in Figure 19, where the effort is linear multiplication of single sample, for higher numbers of samples kept in parallel. Hence, to absorb more energy, one can keep the samples in parallel lattice in desired numbers. The number can be decided by total energy absorption divided by the energy absorption of a single sample.

Conclusion

The detailed experimental and computational studies on the metallic geometrical shape were done. It is learnt that a geometrical shape made up of a combination of the different basic shapes can be utilized for controlled energy absorption. The geometrical parameters of this shape affect their response to loading and their deformation pattern. For example, the less D / t ratio at bottom junction may invoke instability (Figure 14). Moreover, the coefficient of friction plays an important role in this kind of deformation phenomenon. The higher coefficient of friction can be used for the early start of inward inversion in the frusta portion and can prevent inward dimpling of the bottom spherical portion. With higher thickness, the overall energy increases. In addition, the higher thickness invokes early inversion of frusta and stretches this zone (Figure 16).

The simulation was perfected by getting the perfect energy balance equation. The flexibility to model various types of parametric samples with simulation software was utilized. The effect of geometrical, materials, thickness, and other parameters could be studied with these analytical models.
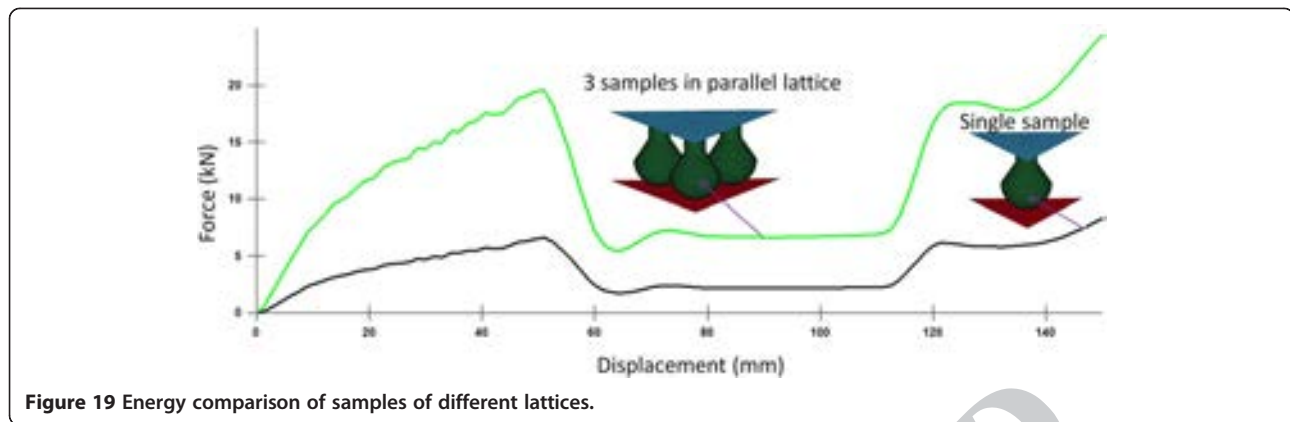

Figure 18 Energy comparison of the samples with different materials.

Figure 19 Energy comparison of samples of different lattices.

Author details
[1]Civil Engineering Department, Indian Institute of Technology Roorkee, Uttarakhand Pin 247667, India. [2]Department of Civil Engineering, Indian Institute of Technology Roorkee, Uttarakhand Pin 247667, India. [3]Engineering Research Centre, Tata Motors-Pune, India.

References
Alghamdi AAA (1991) Design of simple collapsible energy absorber. King Abdulaziz University, Thesis
Alghamdi AAA (2001) Collapsible impact energy absorbers: an overview. Thin-Walled Struc 3(2):189–213
Aljawi AAN, Alghamdi AAA (1999) Investigation of axially compressed frusta as impact energy absorbers. In: Gaul L, Brebbia AA (eds) Computational methods in contact mechanics IV. WIT, Southampton, pp 431–43
Guillow SR, Lu G, Grzebieta RH (2001) Quasi-static axial compression of thin-walled circular aluminium tubes. Int J Mech Sci 43(9):2103–2123
Gupta NK, Mohamed SN, Velmurugan R (2008) Experimental and theoretical studies on buckling of thin spherical shells under axial loads. Int J Mech Sci 50:422–432
Gupta PK (2008) A study on mode of collapse of varying wall thickness metallic frusta subjected to axial compression. Thin-Walled Struc 46:561–571
HyperMesh11 software (2011) A product of Altair Engineering HyperWorks, for fininite element pre-processing. www.altairhyperworks.com, 1820 E Big beavers, Troy, MI 48083
Livermore Software Technology Corporation (2003) LsDyna A program for nonlinear dynamic analysis of structures in three dimension, software and its user manual. Livermore Software Technology Corporation pp 94550–1740: V970
Livermore Software Technology Corporation (2007) LS-PrePost - an advanced pre/post processor for LS-Dyna. Livermore Software Technology Corporation, Livermore, California, pp 94550–1740, V2.1
Mamalis W, Johnson W (1983) The quasi-static crumpling of thin-walled circular cylinders and frusta under axial compression. Int J Mech Sci 25(9/10):713–32
Nia AA, Hamedani JH (2010) Comparative analysis of energy absorption and deformations of thin walled tubes with various section geometries. Thin-Walled Struc 48(12):946–954
Postlethwaite HE, Mills B (1970) Use of collapsible structural elements as impact isolators, with special reference to automotive applications. J Strain Anal 5(1):58–73